

# Diffusion regions and 3D energy mode development in spontaneous reconnection

Shuoyang Wang<sup>1</sup> and Takaaki Yokoyama<sup>1</sup>

*Department of Earth and Planetary Science, The University of Tokyo, Bunkyo-ku, Tokyo 113-0033, JAPAN*

(Dated: 11 June 2019)

The understanding of magnetic reconnection in three-dimension (3D) is far shallower than its counterpart in two-dimension (2D) due to its potential complication, not to mention the evolving of the spontaneously growing turbulence. We investigate the reason for reconnection acceleration on the characters and development of diffusion regions and sheared 3D energy modes (energy modes that are not parallel to the anti-parallel magnetic fields) during the turbulence building stage. We found that multiple reconnection layers emerge due to the growth of 3D sheared tearing instability. Diffusion regions on adjacent reconnection layers form an inflow-outflow coupling that enhances the local reconnection. Further coupling of the existing energy modes breeds new energy modes near the current sheet edge. As reconnection layers span and interact with each other across the whole current sheet, global magnetic energy consumption accelerates. The significant contribution of 3D energy modes and their interaction to the reconnection rate enhancement seems to be independent on magnetic diffusivity. On the other hand, the global guide field changes the layout of 3D reconnection layer thus determines whether the system is fast-reconnection-preferable.

## I. INTRODUCTION

Magnetic reconnection is one of basic nonetheless complicated plasma processes. A reconnecting extensive current sheet spontaneously generates turbulence. The potential non-linear nature of reconnection frequently tangles with turbulence in both macro<sup>1-5</sup> and micro scales<sup>6,7</sup>.

The understanding of the interaction between turbulence and reconnection starts from how turbulence changes the reconnection rate. It was found in two-dimensional (2D) simulation that the global reconnection rate increases by introducing a strong random perturbation onto a current sheet<sup>8</sup>. It was also shown in three-dimensional (3D) simulation that driven turbulence increases the global reconnection rate which becomes independent of diffusivity<sup>1</sup>. The energy of turbulence is applied to the system manually in both cases. How the self-generated turbulence accelerates the reconnection in a free system is not sufficiently understood.

One turbulence reconnection model theoretically describes the reconnection development in a 3D current sheet when a statistical steady turbulent state has reached<sup>9</sup>. In the global scale, which corresponds to the energy input scale, the magnetic fields are absorbed into the global current sheet as the turbulent area expands across the current sheet. In the local scale, which corresponds to the dissipation scale, reconnection happens in the diffusion region and blends the field lines. A fast global reconnection rate is deduced by coupling to the MHD turbulence theory<sup>10</sup> that the local reconnection in local diffusion regions is fast.

Fast overall reconnection is found in 3D spontaneous reconnection. In a current sheet with no guide field, the reconnection rate is shown to be in the magnitude of 0.001, while a non-monotonic change of reconnection rate with diffusivity is found<sup>2</sup>. In a current sheet with a guide field that varies from half to twice of the strength of the anti-parallel fields, the overall reconnection rate is consistently high that  $M_A \sim 0.01$ . This result is found to be independent of diffusivity. The reconnection rate remains high even when the guide field is re-

duced to 10% of the anti-parallel field<sup>4</sup>. Judging by the up-to-date results, it seems that 3D reconnection has the potential to be fast in the system with a large Lundquist number. On the other hand, physics might change with the global guide field strength.

The global features, such as the fast global reconnection rate and the global current sheet expansion<sup>2-5</sup>, are often discussed. The validation of the local reconnection process predicted by the turbulence theory has not been confirmed due to the structural complexity. In addition, the present MHD turbulence theories all consider a strong background field<sup>10-12</sup>. It limits the application of the present turbulence reconnection model. Thus detailed descriptions of both local reconnection in diffusion regions and global behavior are needed to explain more general reconnection picture.

It was speculated that multiple tearing layers might emerge if a multi-modal perturbation is applied to a 3D large sheared magnetic field<sup>13</sup>. In 3D numerical simulations, multiple reconnection layers coexisting in a current sheet built by magnetic shear in large scale are frequently observed<sup>3-5,14-16</sup>. If these reconnection layers are independent of each other, each layer might follow the scenario of 2D plasmoid instability<sup>17-19</sup>. As a whole, they contribute to a global fast reconnection. If the distance between layers is small than their width, these layers might interact with each other. As the interaction is along the sheet width direction (the magnetic shear direction), it should change the plasma and magnetic fields going into the diffusion regions on each layer. In this paper, we execute numerical simulations to understand the development of a spontaneous reconnecting current sheet when multiple reconnection layers emerge. How diffusion regions are affected by the interaction is the main topic.

From our previous study, we noticed an inflow-outflow coupling of flow in a global current sheet with multiple reconnection layers<sup>16</sup>. The coupling is observed as a direct feeding of plasma flow from the outflow region of a diffusion region on one reconnection layer to the inflow region of a diffusion region on another reconnection layer. However, as the initial

perturbation was a random seed of velocity field, it is difficult to extract a detailed analysis of the local diffusion region.

In order to get a clear picture of how diffusion regions on different reconnection layers interact with each other, we apply only 2 reconnection layers in the current sheet from the beginning. This can be achieved by perturbing the current sheet with selected tearing instability eigenfunctions. The inflow-outflow coupling is expected to be built once the pair of reconnection layers are close to each other. By scrutinizing the details of reconnection layer coupling, the physics in the local and global development of diffusion regions is thought to be revealed. The result is believed to compensate for the insufficient detailed description in turbulence reconnection theory<sup>5,9</sup>.

The configuration of this paper is as the following. In Sec.II, we introduce the simulation model and setup. In Sec.III, the local and global detailed analyses of a typical tearing-eigenfunction-perturbed simulation are presented, followed by the result of a parameter survey of changing tearing mode wavelength. In Sec.IV, the result found in the previous section is reexamined in random-perturbed systems with various diffusivities and strengths of the global guide field. In Sec.V, discussion on the extension of our present result is shown. Final conclusion is summarized in Sec.VI.

## II. SIMULATION MODEL

We apply ordinary one-fluid resistive (uniform diffusivity) MHD equations which neglect viscosity, gravity and heat conduction for simplicity, together with the equation of state for the ideal gas:

$$\frac{\partial \rho}{\partial t} + (\mathbf{v} \cdot \nabla) \rho = -\rho(\nabla \cdot \mathbf{v}) \quad (1)$$

$$\rho \frac{\partial \mathbf{v}}{\partial t} + \rho(\mathbf{v} \cdot \nabla) \mathbf{v} = -\nabla p + \frac{\mathbf{J} \times \mathbf{B}}{c} \quad (2)$$

$$\rho \frac{\partial e}{\partial t} + \rho(\mathbf{v} \cdot \nabla) e = -p \nabla \cdot \mathbf{v} + \eta \mathbf{J}^2 \quad (3)$$

$$\frac{\partial \mathbf{B}}{\partial t} = \nabla \times (\mathbf{v} \times \mathbf{B} - c \eta \mathbf{J}) \quad (4)$$

$$\mathbf{J} = \frac{c}{4\pi} \nabla \times \mathbf{B} \quad (5)$$

in which  $\rho$  and  $p$  are plasma mass density and pressure,  $\gamma = 5/3$  is the adiabatic index,  $e$  is the internal energy per unit mass that  $e = p/[(\gamma - 1)\rho]$  and  $\eta$  is the resistivity.

All quantities are normalized by the typical parameters. The length scale is in the unit of the initial current sheet width  $\delta$ . The time scale is normalized by  $t_A = \delta/v_{A0}$ , where  $v_{A0}$  is the asymptotic Alfvén velocity. Initial uniform mass density  $\rho_0$  is used for normalizing mass density. Normalization of the magnetic field is implemented by  $B_0 = v_{A0}\sqrt{\rho_0}$ . Current density is normalized by  $J_0 = cB_0/\delta$  while plasma pressure is normalized by  $p_0 = B_0^2$ . All equations are solved in Cartesian coordinate.

Our background magnetic field is composed of anti-parallel

component  $B_y(x)$  with a uniform finite guide field  $B_z$ :

$$\begin{aligned} \mathbf{B} &= B_y \hat{\mathbf{y}} + B_z \hat{\mathbf{z}} \\ &= B_{y0} \tanh\left(\frac{x}{a}\right) \left\{ \frac{1}{2} \left[ \tanh\left(\frac{|x| - 4\delta}{a}\right) - 1 \right] \right\} \hat{\mathbf{y}} \\ &\quad + \alpha B_{y0} \hat{\mathbf{z}} \end{aligned} \quad (6)$$

where  $B_{y0} = \sqrt{4\pi}B_0$  and  $a = 0.5\delta$ . This modified Harris sheet has one central global current sheet centered at  $x = 0$  and two secondary current sheets near  $x = \pm 4\delta$ . This configuration is to simplify the boundary condition across the current sheet direction, while the secondary current sheets do not participate in reconnection essentially within our simulation time. The guide field strength is mediated by parameter  $\alpha$ . To obtain a static global structure, the total uniform pressure is set as:

$$P_{\text{tot}} = \frac{B_0^2}{2} (1 + \alpha^2)(1 + \beta) \quad (7)$$

in which  $\beta = 0.2$  is the ratio between the plasma pressure and the magnetic pressure at the asymptotic field outside of the central global current sheet.

We divide the simulations into two groups regarding the different forms of the perturbation onto the initially static central global current sheet. Other parameters are also changed for a more general scan.

We denote the first simulation group as the eigenmode-perturbation simulation group. The simulations in this group are triggered by velocity and magnetic fields of selected tearing mode eigenfunctions. They are used to understand the basic development of the reconnection layer interaction. In this group, two subgroups of simulations are included to make comparisons.

The first subgroup, called double-layer simulation, is perturbed by two superposed tearing modes  $\mathbf{k}_L$  and  $\mathbf{k}_R$ . These two modes are 3D tearing modes which are shear to the global anti-parallel magnetic field. The perturbation results in the emergence of one reconnection layer on either side of the central global current sheet from the beginning of the simulation (similar to Grasso, Borgogno, and Pegoraro<sup>20</sup>).

To simplify the analysis, the two modes  $\mathbf{k}_L$  and  $\mathbf{k}_R$  are chosen to be rotational-symmetric across the central global current sheet center. The initial fields become

$$\mathbf{B}(t=0) = \mathbf{B}^{[0]} + \mathbf{B}_L^{[1]} + \mathbf{B}_R^{[1]} \quad (8)$$

$$\mathbf{v}(t=0) = \mathbf{v}_L^{[1]} + \mathbf{v}_R^{[1]}, \quad (9)$$

where [0] and [1] represent background and first-order perturbation components of fields. The amplitude of the initial perturbation is determined that

$$\max(|v_x|, |v_y|, |v_z|) = 0.01 v_{A0}. \quad (10)$$

This amplitude is small enough to start from the linear stage but large compared to many other studies. Since what we are interested in is the nonlinear interaction between the two reconnection layers, by applying appropriately large initial amplitude, the system enters the nonlinear stage earlier that the simulation resource is saved.

The other subgroup, called single-layer simulation, is perturbed by one single 3D tearing mode  $\mathbf{k}_R$  that only one reconnection layer emerges on the positive- $x$  side of the central global current sheet. The initial fields are

$$\mathbf{B}(t=0) = \mathbf{B}^{[0]} + \mathbf{B}_R^{[1]} \quad (11)$$

$$\mathbf{v}(t=0) = \mathbf{v}_R^{[1]}. \quad (12)$$

This group of simulations is used to differentiate the reconnection layer interaction result from the potential nonlinear development of a single tearing mode.

We label each tearing mode as  $(m, n)$ . The integers  $m$  and  $n$  are defined by the box size  $L_y$  and  $L_z$  along  $y$ - and  $z$ -direction respectively that

$$m = k_y \frac{L_y}{2\pi} \quad (13)$$

$$n = k_z \frac{L_z}{2\pi}, \quad (14)$$

where  $k_y$  is always positive while  $k_z$  can be positive or negative. In our system, the mode growing on the negative- $x$  side is labeled as  $n < 0$  while the mode growing on the positive- $x$  side is labeled as  $n > 0$ . Therefore, double-layer simulations are labeled in the form of  $(m, \pm|n|)$  while single-layer simulations are labeled as  $(m, |n|)$ . As a tearing mode  $(m, n)$  grows, its correspondent energy mode  $(m, n)$  also grows.

The tearing instability grows on the layer where

$$\mathbf{B} \cdot \mathbf{k} = 0 \quad (15)$$

is satisfied. As the tearing instability grows, the layer gradually grows into a reconnection layer. We define a resonance factor  $q$  that

$$q = \frac{B_y(x)}{B_z}, \quad (16)$$

which mimics the safety factor used in a tokamak or a reversed-field pinch (RFP). On a reconnection layer with a certain  $q$ , a series of harmonics grows with the same ratio of  $n/m$  that

$$q = -\frac{L_y n}{L_z m}. \quad (17)$$

By combining Eq.(16) and Eq.(17), the resonance condition determines the reconnection layer position  $x_s$  along the  $x$ -direction in the initial central sheared magnetic fields:

$$x_s \sim \alpha a \frac{L_y n}{L_z m} \quad (18)$$

for a certain tearing mode  $(m, n)$  and its correspondent energy mode  $(m, n)$ .

The tearing modes we apply as  $\mathbf{k}_R$  are  $(1, 1)$ ,  $(2, 1)$ ,  $(3, 1)$ ,  $(4, 1)$  for the two subgroups. Their rotational-symmetric counterparts are also applied as  $\mathbf{k}_L$  in the double-layer simulation subgroup. Among them, we select the tearing mode  $(3, 1)$  as the typical mode to investigate the reconnection layer interaction across the sheet. In all these simulations,

the guide field strength  $\alpha = 0.1$  and the diffusivity  $\tilde{\eta} = \eta c^2 / (4\pi) \sim 3.2 \times 10^{-4} \delta^2 / t_A$  are used. The double-layer simulation  $(3, \pm 1)$  continues until the boundary is influencing the central global current sheet ( $\sim 640 t_A$ ). The other simulations stop at  $\sim 200 t_A$ . All single-layer simulations maintain a translational-invariance along  $\mathbf{k}_R$  until the end of simulations.

The second simulation group is denoted as the random-perturbation simulation group. It is used to confirm the result achieved from the eigenmode-perturbation simulations. The simulations in this group are triggered by a random velocity field with an amplitude the same as Eq.(10). We separate the simulations into two subgroups. In one subgroup, we vary the guide field strength  $\alpha$  from 0.01 to 0.2, while the diffusivity is kept the same as the eigenmode-perturbation simulation group ( $\tilde{\eta} = 3.2 \times 10^{-4} \delta^2 / t_A$ ). In another subgroup, we test three cases of simulation with different diffusivity  $\tilde{\eta} = 1.6, 3.2$  and  $6.5 \times 10^{-4} \delta^2 / t_A$ , while the guide field is the same as the eigenmode-perturbation simulation group ( $\alpha = 0.1$ ). The Lundquist number  $S$  in our system is defined by the total Alfvén speed  $v_A = v_{A0} \sqrt{1 + \alpha^2}$  that  $S = v_A L / \tilde{\eta} \sim 0.3, 0.7$  and  $1.3 \times 10^5$ , respectively for the subgroup with different diffusivity. All simulations in this group continue until the current sheets at the boundary impact strongly to the central global current sheet (roughly  $700 t_A \sim 900 t_A$ ). We stop the simulation of  $\alpha = 0.01$  case in the random-perturbation simulation group at  $t = 1000 t_A$  as we are interested in the global current sheet development in the same time range.

In all simulations, the simulation box has a periodic boundary condition on all sides. The box size is  $L_x \times L_y \times L_z = 10\delta \times 24\delta \times 6\delta$ , which is resolved by  $640 \times 1000 \times 250$  grids at least. Across the  $x$ -direction, we apply non-uniform grids to resolve the central global current sheet that  $\Delta x \geq 0.005\delta$ . Uniform grids along  $y$ - and  $z$ -direction are adjusted with  $\Delta y = \Delta z = 0.024\delta$ . In double-layer simulation  $(4, \pm 1)$  and its single-layer counterpart,  $\Delta x \geq 0.004\delta$  and  $\Delta y = \Delta z = 0.015\delta$  are used. For the higher Lundquist number case,  $\Delta x \geq 0.0025\delta$  and  $\Delta y = \Delta z = 0.015\delta$  are used. Resolution check is done by applying different widths of current sheet in solving 1D diffusion equation. The grid size we apply here could resolve the diffusion region with a thickness of at least  $a = 0.02\delta$ . We test the convergence check by changing the grid size into  $\Delta y = \Delta z = 0.04\delta$  for the double-layer simulation  $(1, \pm 1)$ . At  $t = 100 t_A$ , the reconnection rate increases by 3%. The typical structures are not essentially changed, only the local reconnection is reduced moderately in the higher resolution simulation. So we argue that the resolution does not have a strong impact on our model, however the scaling might be changed when an even higher resolution is applied. We use CIP-MOCCT code<sup>21</sup> with artificial Lapidus-type viscosity<sup>22</sup> developed by H. Isobe from Kyoto University.

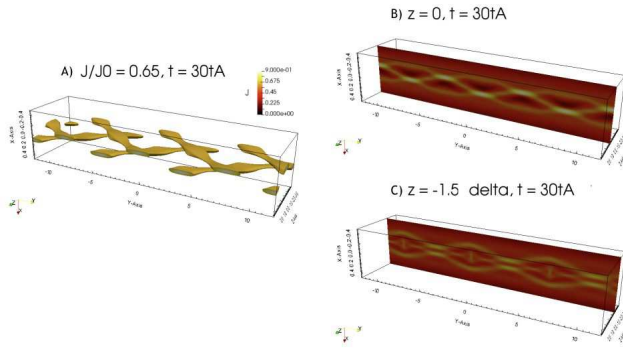


FIG. 1. 3D structures of the double-layer simulation  $(3, \pm 1)$  at  $t = 30t_A$ . Bright features represent diffusion regions. Panel A): current density isosurface  $J/J_0 = 0.65$ . Panel B): current density  $J$  on  $z = 0$  plane. Panel C): current density  $J$  on  $z = -1.5\delta$  plane.

### III. SIMULATION RESULT I: EIGENMODE-PERTURBATION GROUP

#### A. Typical case: double-layer simulation $(3, \pm 1)$

We specifically study the development of the double-layer simulation  $(3, \pm 1)$  as a typical case. The reconnection layer of the tearing mode  $(3, 1)$  locates close to the current sheet center that it can build an efficient interaction with its counterpart across the central global current sheet. Moreover, the tearing mode  $(3, 1)$  is one of the most unstable 3D tearing modes in our system. It is expected to be dominant in the linear phase.

##### 1. Local analysis of inflow-outflow coupling

After simulation starts, two reconnection layers emerge. The isosurface of the current density  $J$  is plotted in Fig.1 panel A). The diffusion regions are defined as the regions with high current density, which are the bright features in Fig.1. Meanwhile, converging inflows and diverging outflows are identified in the enhanced current density region. The diffusion regions form lines along the sheet direction. They are parallel to the local  $\mathbf{B}$  and perpendicular to  $\mathbf{k}$  of the correspondent tearing mode. Since  $\mathbf{k}$  on either side of the current sheet are different, the alignment of diffusion regions changes on different  $z$ -plane. Two characteristic alignment structures are shown in panels B) ( $z = 0$ ) and C) ( $z = -1.5\delta$ ). In panel B), tearing modes on either side has a phase shift of  $\pi$  along the current sheet ( $y$ -direction), while in panel C) the phase shift is  $\pm\pi/2$ . We denote the planes similar to  $z = 0$  and  $z = -1.5\delta$  as anti-symmetric and symmetric planes, respectively.

As can be seen in Fig.1, the system varies from the anti-symmetric plane to the symmetric plane periodically if each  $z$ -plane is scanned along the global guide field direction. We assume that the regions in between the anti-symmetric and the symmetric planes are possessing the characters from both of these planes. So in the following part, we concentrate on the development of these two characteristic planes and treat the other planes as a mixture.

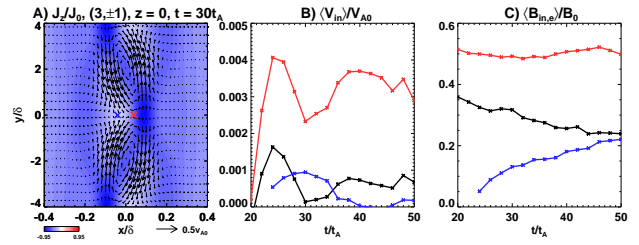


FIG. 2. Panel A): the inflow-outflow coupling in the double-layer simulation  $(3, \pm 1)$  at  $t = 30t_A$ . One wavelength is presented along the  $y$ -direction. The velocity field on  $z = 0$  plane is plotted as vectors over the contour plot of current density  $J_z/J_0$ . The positions of plasma inflow and upstream magnetic field measurement on  $y = 0$  line are labeled by thick red and blue crosses. Panel B): spatially averaged plasma inflow into the diffusion region on the reconnection layer of the tearing mode  $(3, 1)$ . Panel C): spatially averaged upstream magnetic field into the diffusion region on the reconnection layer of the tearing mode  $(3, 1)$ . Red and blue lines with crosses are measurements on the anti-symmetric and symmetric planes in the double-layer simulation  $(3, \pm 1)$  respectively. Black lines with crosses are measurements in the single-layer simulation  $(3, 1)$ . The values are shown in the time range when diffusion regions can be identified and maintain intact.

The anti-symmetric plane is in favor of inflow-outflow coupling. A typical inflow-outflow coupling on  $z = 0$  plane in the double-layer simulation  $(3, \pm 1)$  is shown as the velocity vectors in panel A) of Fig.2. The diffusion regions are described as being coupled when the inflow-outflow coupling is built by them. To understand how the inflow-outflow coupling changes the local reconnection more quantitatively, we study the reconnection characters of a coupled diffusion region on an anti-symmetric plane ( $z = 0$ ). The diffusion region is selected to be on the reconnection layer of the tearing mode  $(3, 1)$  (on the positive- $x$  side) and lays across  $y = 0$  line.

We first calculate the current density  $J_\perp$  that is perpendicular to  $\mathbf{k}_R$ . Then we find the local minimum  $J_{\perp, \min}$  along  $y = 0$  line. The size of the diffusion region is closed by the positions where  $J_\perp$  is half of  $J_{\perp, \min}$ . The plasma flows converge into the left and right diffusion region boundaries along  $x$ -axis are considered as the inflows. The flows diverge out from the upper and lower diffusion region boundaries along  $y$ -axis are considered to be the outflows. The length of a diffusion region is defined as the distance between the upper and lower boundaries along  $\mathbf{k}_R$ . The inflow characters along the left boundary of the diffusion region we choose are influenced by the inflow-outflow coupling. The position of this boundary on  $y = 0$  line is labeled as the red cross in panel A). We average the inflows spatially along a line that centers at this point and extends along  $\mathbf{k}_R$  in a length of the diffusion region length.

We also measure the magnetic field  $B_\parallel$  that is parallel to  $\mathbf{k}_R$  in the position where the current density  $J_\perp$  is roughly 0 to the left of the diffusion region inflow boundary. As the frozen-in condition is satisfied, the measured magnetic field is considered to be the upstream magnetic field of the reconnection in this coupled diffusion region. The position of the measurement on  $y = 0$  line is labeled as the blue cross in panel A). The magnetic field is averaged along the line that centers at

this point and extends along  $\mathbf{k}_R$  in a length of the diffusion region length.

The normalized spatially averaged inflows  $\langle V_{in} \rangle / V_{A0}$  are plotted in panel B) of Fig.2. It can be seen that the local inflow into the diffusion region is enhanced by roughly 6 times on the anti-symmetric plane in the double-layer simulation compared to that in the single-layer simulation. The inflow into the diffusion region on the symmetric plane is initially comparable as that in the single-layer simulation. It decreases with time and falls to roughly one-quarter of the measurement in the single-layer simulation around  $t = 50t_A$ . The result directly shows that the inflow-outflow coupling contributes to the local reconnection acceleration.

The normalized spatially averaged upstream magnetic fields  $\langle B_{in,e} / B_0 \rangle$  are plotted in panel C), which shows another effect of the inflow-outflow coupling. As the inflow increases, the magnetic field is transported fast into the diffusion region thus piles up in front of the inflow region. It is shown that the upstream magnetic field of the diffusion region on the anti-symmetric plane in the double-layer simulation is roughly twice of that in the single-layer simulation at  $t = 50t_A$ . In the single-layer simulation, the upstream magnetic field gets weaker as the reconnection saturates. Reversely, the upstream magnetic field of the diffusion region on the symmetric plane is growing. It is probably because that the reconnection in the diffusion region saturates so fast that it cannot consume all magnetic fields that are transported into it previously. Thus a piling up of magnetic flux is observed.

Theoretically, secondary tearing is triggered when  $\Delta'$  is large<sup>18,23</sup>. It means a strong piling-up magnetic field in front of the diffusion layer. Therefore, secondary tearing is expected to grow when the inflow-outflow coupling is effective, as the upstream magnetic field accumulates. In Fig.3, we track the diffusion region development on the anti-symmetric and symmetric planes in the double-layer simulation  $(3, \pm 1)$  and on the  $z = 0$  plane in the single-layer simulation  $(3, 1)$  along time. At  $t = 100t_A$  in the double-layer simulation  $(3, \pm 1)$ , secondary tearing feature is observed on the anti-symmetric plane in A2). No such feature is found on the symmetric plane in the double-layer simulation  $(3, \pm 1)$  or in the single-layer simulation  $(3, 1)$ . The diffusion region on the symmetric plane shrinks without splitting, as can be observed from B1) to B3). The diffusion region in the single-layer simulation extends and saturates as the current density becomes weaker from C1) to C4). From the information above, it can be seen that the secondary-tearing-like feature in  $(3, \pm 1)$  is not an intrinsic character of the tearing mode  $(3, 1)$  but rather a result from the interaction of reconnection layers.

Secondary tearing is an indication of a further violent change of a current sheet, as shown in the plasmoid instability<sup>18,19,24–26</sup>. Unlike the plasmoid instability, which comes from the interaction between diffusion regions and plasmoids along a single current sheet, the inflow-outflow coupling in 3D is in the direction across the global current sheet. The coupling can be only built when there exists a phase shift of tearing modes. It reflects the importance of understanding the three-dimensionality in the reconnection study.

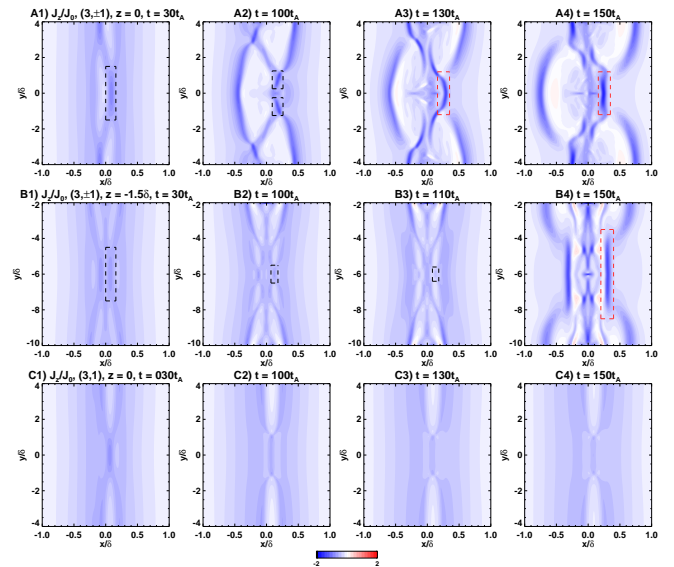


FIG. 3. Current density contour plot on anti-symmetric plane  $z = 0$  (upper panels) and symmetric plane  $z = -1.5\delta$  (middle panels) in the double-layer simulation  $(3, \pm 1)$  and  $z = 0$  plane in the single-layer simulation  $(3, 1)$  along time. The original diffusion regions are labeled by black boxes with dashed lines, while new diffusion regions are labeled by red boxes with dashed lines. Only one period along  $y$ -direction is shown.

In the plasmoid instability, diffusion regions are incessantly produced during the violent phase. From Fig.3, it can be found that new diffusion regions are created. In addition to the partition of the original diffusion region in A2), a new overlying diffusion region starts to grow outside on the anti-symmetric plane in the double-layer simulation  $(3, \pm 1)$ . It becomes more visible with time and seems to dominate the reconnection at  $t = 150t_A$  in A4). The production of the overlying diffusion region on the anti-symmetric plane is likely to relate with the partitioned diffusion regions. As two diffusion regions are produced as A2) shows, their sheet-wise outflows have a head-on collision and diverge. The diverging flow along positive- $x$  carries the magnetic fields outwardly and meet the free field lines that are going inwardly under the global Lorentz force. The squeeze then creates the new diffusion region.

A new overlying diffusion region is also identified outside of the original one on the symmetric plane at  $t = 150t_A$  in B4). Its production mechanism is thought to be different from that on the anti-symmetric plane. Because no new diffusion region is found in the single-layer simulation  $(3, 1)$ , the production should be related to the interaction of reconnection layers.

## 2. Global development of reconnection layer coupling

The creation of diffusion regions outwardly to the initial diffusion regions on both characteristic planes at  $t = 150t_A$  suggests that the production is a global trend. The current density isosurface  $J/J_0 = 0.6$  in the whole simulation box is plotted in Fig.4 to show the global picture. The wavy struc-

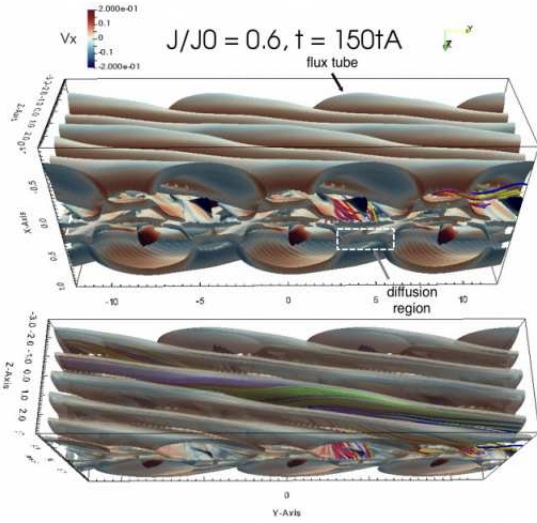


FIG. 4. Current density isosurface represents flux tube boundaries and diffusion regions in the whole simulation box. Yellow, purple and green lines are selected magnetic field lines from  $z = 0, -1.2\delta$  and  $1.2\delta$  planes, while red and blue lines are selected magnetic field lines on  $z = -0.6\delta$  and  $0.6\delta$  planes. All lines root along the layer corresponds to energy mode  $(3, -5)$ .

tures are boundaries of flux tubes. There is one group of flux tubes on either side of the central global current sheet. They extend along the sheet direction. The orientation of these flux tubes indicates the growth of new energy modes  $(3, 5)$  and  $(3, -5)$ , which are growing on different  $x$ -planes compared to the initial energy modes  $(3, 1)$  and  $(3, -1)$ . By plotting the magnetic field lines that root on the layer corresponds to the energy mode  $(3, -5)$ , it can be seen that these lines are twisting with each other and confined inside the flux tube. Since these flux tubes cover large areas along global sheet direction, they are created by a reconnection layer respectively. Therefore, it is proved that new diffusion regions are created globally and form a new reconnection layer on either side of the central global current sheet.

The layers on which energy mode  $(3, 5)$  and  $(3, -5)$  grow are closer to the asymptotic magnetic fields than the initial energy modes  $(3, 1)$  and  $(3, -1)$  by applying Eq.(18). They are capable to transport the magnetic fields with large magnetic energy into the global current sheet central region to be dissipated. If inflow-outflow couplings still exist in this stage to support a fast local reconnection, the global reconnection is expected to increase compared to the case when all reconnection layers are closer to the global central current sheet center.

We first calculate the total kinetic energy in the box and the overall magnetic energy dissipation rate. The total kinetic energy is calculated as:

$$E_k = \int_{-\frac{L_x}{2}}^{\frac{L_x}{2}} \int_{-\frac{L_y}{2}}^{\frac{L_y}{2}} \int_{-\frac{L_z}{2}}^{\frac{L_z}{2}} \frac{1}{2} \rho \mathbf{v}^2 dx dy dz. \quad (19)$$

The overall magnetic energy dissipation rate is calculated by

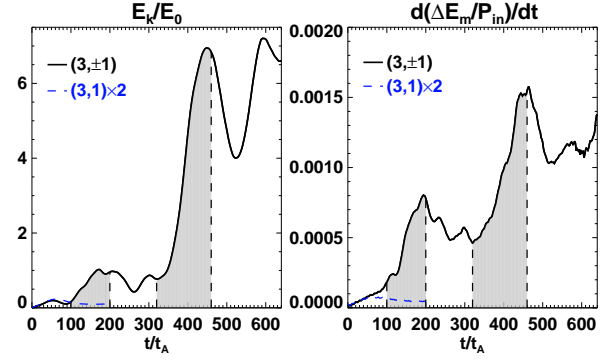


FIG. 5. The total kinetic energy (left) and the overall magnetic energy dissipation rate (right) of the double-layer simulation  $(3, \pm 1)$ . The periods in which the magnetic energy dissipation rate has a boost are shaded by gray. The normalized result from the single-layer simulation  $(3, 1)$  until  $t = 200t_A$  is also plotted as the blue dashed lines.

the time derivative of the reduced total magnetic energy:

$$\Delta E_m = \int_{-\frac{L_x}{2}}^{\frac{L_x}{2}} \int_{-\frac{L_y}{2}}^{\frac{L_y}{2}} \int_{-\frac{L_z}{2}}^{\frac{L_z}{2}} \frac{|\mathbf{B}_f|^2 - |\mathbf{B}|^2}{8\pi} dx dy dz, \quad (20)$$

where  $\mathbf{B}_f$  is the magnetic field calculated in a nonlinear simulation without any perturbation. By subtracting  $\mathbf{B}_f$ , the magnetic change from the global diffusion is removed. The overall magnetic energy dissipation rate is normalized by  $P_{in} = 2L_y L_z v_{A0} B_{y0}^2 / (4\pi)$ . It represents the total inflow Poynting flux estimated by the global asymptotic magnetic field from both sides of the central global current sheet.

By observing the total kinetic energy and the overall magnetic energy dissipation rate in Fig.5, we notice two boosts in the two shaded periods ( $t = 100 - 200t_A$  and  $t = 320 - 460t_A$ ). In comparison, no such eruptive energy release is observed in the single-layer simulation  $(3, 1)$ .

The overall magnetic energy dissipation rate boosts suggest faster local reconnection in these periods, which can be achieved by inflow-outflow couplings from our analysis in Sec.III A 1. In order to build inflow-outflow couplings across the sheet direction, multiple reconnection layers that span across the sheet direction should coexist in the central global current sheet. Thus multiple energy modes with large enough amplitude to participate in reconnection on these layers are required.

We calculate the magnetic energy of each mode  $(m, n)$  in the Fourier space by converting the magnetic field

$$\tilde{\mathbf{B}}(x, m, n) = \frac{1}{L_y L_z} \int_{-\frac{L_x}{2}}^{\frac{L_x}{2}} \int_{-\frac{L_y}{2}}^{\frac{L_y}{2}} \mathbf{B}(x, y, z) e^{-i(k_y y + k_z z)} dy dz \quad (21)$$

into magnetic energy spectrum and integrate along the  $x$ -direction that

$$\tilde{E}_m(m, n) = \int_{-\frac{L_x}{2}}^{\frac{L_x}{2}} \frac{|\tilde{\mathbf{B}}(x, m, n)|^2}{8\pi} dx \quad (22)$$

to track the dominant energy mode growth along time. Since we are applying the rotational-symmetric setup, we average

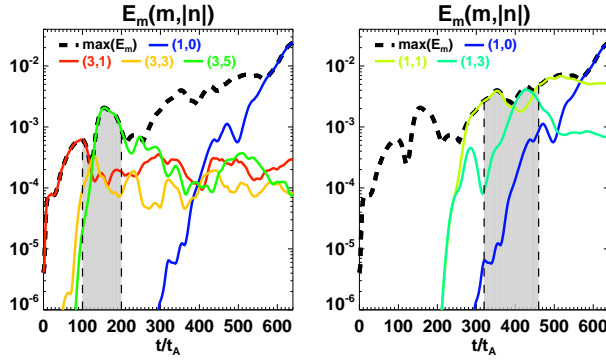


FIG. 6. Dominant magnetic mode energy in the selected periods (shaded by gray colors) which correspond to the overall magnetic energy dissipation rate boosts in Fig.5. Black dashed line is the maximum mode energy at each time step ((0,0) mode excluded). Colored lines are the most energetic modes during each boost. An overlap of a color line with the black dashed line means that this mode is the dominant mode at this moment. The energy mode (1,0) is also plotted as blue lines.

all energy modes in the form of

$$\tilde{E}_m(m, |n|) = \frac{1}{2} [\tilde{E}_m(m, +|n|) + \tilde{E}_m(m, -|n|)] \quad (23)$$

for convenience.

Selected energy modes are plotted in Fig.6. The periods shaded by gray correspond to the same periods in Fig.5. A selected mode is the energy mode which grows over other modes, namely becomes the most energetic mode, in the gray shaded regions. The 3D modes (i.e., modes with  $n \neq 0$ ) always dominate during the two boosts periods. Inside the first shaded period ( $t = 100 - 200t_A$ ), the most energetic mode changes from the initially grown energy mode (3,1) to (3,3) then finally (3,5). It shows a shift from an energy mode with a smaller  $|n|$  to an energy mode with a larger  $|n|$ . Thus it indicates a creation of reconnection layer outwardly. On the right panel, we plot the most energetic modes in the second shaded period ( $t = 320t_A - 460t_A$ ). Before entering this phase, the system seems to undergo a re-organization. The energy mode (1,1), which is closer to the central global current sheet center than its predecessor (3,5), grows rapidly. It corresponds to a coalescence-like process. The energy mode (1,3) grows fast after energy mode (1,1). It also shows an increase of only  $|n|$  value thus new reconnection layers grow externally. Since the difference of the most energetic modes strength in the shaded periods is within 1 order of magnitude, it implies the coexistence of multiple reconnection layers in the central global current sheet.

None of the successive energy modes in the shaded periods is preferred by the initially static system. It means that they must grow by receiving energy from the existing energy modes by nonlinear process<sup>27</sup>. We refer to this mechanism as the nonlinear coupling of two energy modes  $(m_1, n_1)$  and  $(m_2, n_2)$  in the following context, which can be described as

$$(m_1, n_1) + (m_2, n_2) \rightarrow (m_1 \pm m_2, n_1 \pm n_2) \quad (24)$$

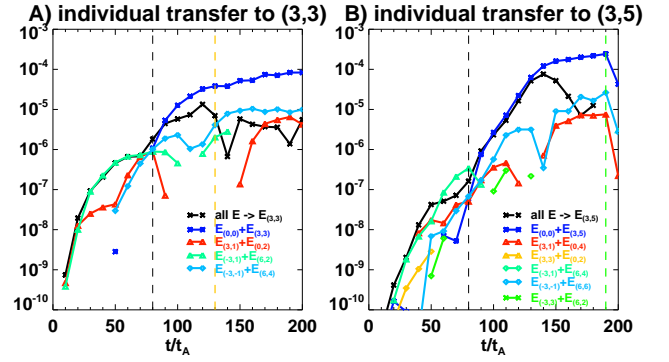


FIG. 7. The individual energy transfer rates of energy modes (3,3) and (3,5) from different paths. Black dashed lines ( $t = 80t_A$ ) are the starting time for the rapid growth of energy modes (3,3) and (3,5). Orange ( $t = 130t_A$ ) and green dashed lines ( $t = 190t_A$ ) label the peak times for the dissipation rate of these two modes respectively.

in general. Chain effect of successive nonlinear coupling between daughter and mother energy modes will spread out an extended energy spectrum. We calculate the energy transfer rate along each path to find the most contributing one that explains the emergence of new energy modes in the shaded periods of Fig.6. We skip the second shaded region as the whole system becomes so turbulent that the energy mode is less well-defined. The calculation of the energy transfer rate is based on the study by Dahlburg, Antiochos, and Zang<sup>28</sup>, which is the extension of the work in hydrodynamics<sup>29</sup>.

The individual energy transfer paths of energy modes (3,3) and (3,5) are showed in Fig.7. Before the rapid growth from  $\sim 90t_A$ , the main energy transfer paths into the energy mode (3,3) are  $(3,1) + (0,2)$ ,  $(-3,1) + (6,2)$  and  $(-3,-1) + (6,4)$ . The first transfer path can be understood by geometric confinement. The second and the third transfer paths both involve higher wavenumber modes. Energy mode (6,2) is the second harmonic of the original energy mode. Energy mode (6,4) is produced predominantly by  $(-3,1) + (9,3)$  (not shown) and energy mode (9,3) is the third harmonic of the original mode. Similar processes happen for energy mode (3,5). The energy transfer path  $(-3,1) + (6,4)$  dominates before (3,5) grows rapidly. In addition, the second harmonic of energy mode (3,3) is also participating in transferring the energy via  $(-3,-1) + (6,6)$ .

A general trend in both cases is that the new energetic mode in the positive- $x$  side is mainly charged by the nonlinear coupling of the present strongest energy mode in the negative- $x$  side and higher harmonics (and its product) modes in the positive- $x$  side (turquoise lines). On the other hand, the growth of higher order harmonics of the original energy modes is related to the secondary tearing. As the secondary tearing is triggered by the inflow-outflow coupling between the initial energetic modes, it is suggested here that the inflow-outflow coupling and the nonlinear coupling are related processes.

After  $80t_A$ , the energy transfer from energy mode (0,0) becomes predominant for both modes. It runs over the total energy transfer from  $90t_A$  in growing energy mode (3,3) and

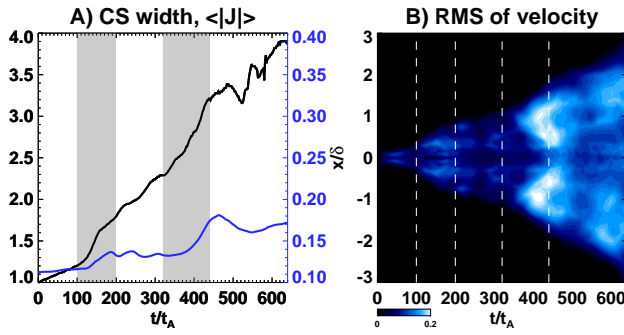


FIG. 8. Panel A): the central global current sheet width (black line) and the spatially averaged current density (blue line) in the whole simulation box. Panel B): root-mean-square of the velocity field along the  $x$ -direction. The two boost periods are shaded by gray in panel A) and in between the dashed lines in panel B).

$140t_A$  in growing energy mode  $(3, 5)$ , since these two modes are pouring energy to other modes as well. It implies that these two energy modes are growing mainly by absorbing energy from the background current after they are charged by other modes to a large enough amplitude, similar to an ordinary tearing mode.

As new energy modes are activated near the sheet edge due to the nonlinear coupling, the reconnection layers span from one side of the central global current sheet to the other side. By a direct observation of local flow pattern and diffusion region distribution, an increasing number of inflow-outflow coupling event can be found inside the central global current sheet during the shaded periods. Therefore, a 3D web-like energy consuming engine is formed by connecting magnetic fields from either side of the sheet, where magnetic energy is abundant, through multiple layers in between. As the layer extends along the sheet and the local reconnection is fast due to the inflow-outflow coupling, a global fast reconnection is achieved when new layers are formed near the edges (Fig.5).

To consolidate our argument that 3D modes are important in the 3D reconnection, we plot the spatially averaged current density strength  $\langle |J| \rangle$

$$\langle |J| \rangle = \int_{-L_z/2}^{L_z/2} \int_{-L_y/2}^{L_y/2} \int_{-L_x/2}^{L_x/2} |\mathbf{J}(x, y, z)| dx dy dz / (L_x L_y L_z) \quad (25)$$

and central global current sheet width in panel A) of Fig.8. The central global current sheet width is defined as the distance between the positions with a certain current density threshold that equals to the current density at the initial current sheet half-width ( $\sim 0.24J_0$ ).

Inside the shaded periods which correspond to the reconnection boosts, there exist faster expansions of the current sheet. Meanwhile,  $\langle |J| \rangle$  increases during these phases. It also indicates an acceleration of global dissipation. During the re-organization phase, the current sheet also expands. It is mainly due to the coalescence-like process that larger flux tubes are created. The expansion speed in the re-organization phase is roughly half compared to the fast expansion in the two shaded periods.

In panel B), we plot the root-mean-square of the total velocity  $v_{\text{rms}}$  along  $x$ -direction. The main contribution to the total velocity is  $v_y$ , which is the outflow from diffusion regions. It can be seen that  $v_{\text{rms}}$  increases during two boost periods. Meanwhile, the enhancement is off from the central global current sheet center as they are mainly the outflow from the 3D modes.

From all arguments above, we found how important 3D energy modes are for the whole development of the 3D reconnection picture by exploring details in one simulation result. In the following part, our arguments are rechecked in various conditions to get a general conclusion.

## B. Parameter survey of inflow-outflow coupling

In this section, we examine the dependence of the local reconnection enhancement due to the inflow-outflow coupling on the layer distance. In addition, we check the generality of our results on the global development. The double-layer simulations used in this section are  $(1, \pm 1)$ ,  $(2, \pm 1)$ ,  $(3, \pm 1)$  and  $(4, \pm 1)$ . Their single-layer simulation counterparts are also included for comparison.

In our system, changing  $\mathbf{k}$  will change both the reconnection layer position  $x_s$  and the tearing mode wavelength  $\lambda$ . Because the inflow region size is positively scaled to the wavelength<sup>30</sup>, we normalize the layer distance  $d_l$  to  $\lambda$  and define a normalized layer distance  $A_c$ :

$$A_c = \frac{d_l}{\lambda} \sim \frac{2\alpha n}{L_z} \sqrt{1 + \left(\frac{nL_y}{mL_z}\right)^2} \quad (26)$$

where  $d_l$  is evaluated by Eq.(18). By this definition, the double-layer simulation  $(4, \pm 1)$  has the smallest  $A_c$  value while  $(1, \pm 1)$  has the largest  $A_c$ . We check the inflow enhancement dependence on the value of  $A_c$  in the following part. The diffusion region on the layer produced by the tearing mode  $(m, 1)$  and locates across  $y = z = 0$  line (similar to Sec.III A 1).

We measure the inflow strength on both sides of the diffusion region on  $z = 0$  plane in all simulations. The inflow measuring position is similar to that in Sec.III A 1. The measurements are averaged along  $\mathbf{k}_R$  in a length half of the diffusion region length, then averaged along time from when the flow becomes steady until secondary tearing starts to grow. The inflow from the left side of the diffusion region is the inflow involved in the inflow-outflow coupling in a double-layer simulation. The inflow from the right side of the diffusion region does not participate in the inflow-outflow coupling. The result is shown in Fig.9.

The inflow measured from the left side increases monotonically in panel A) when the reconnection layers are closer to each other. In order to see how much the inflow from the left side enhances due to the inflow-outflow coupling, we normalize the inflow in the double-layer simulations to their single-layer counterparts and plot it in panel B). The inflow enhancement also shows a monotonic increase with decreasing layer distance. It is worth pointing out that the inflow ratio for



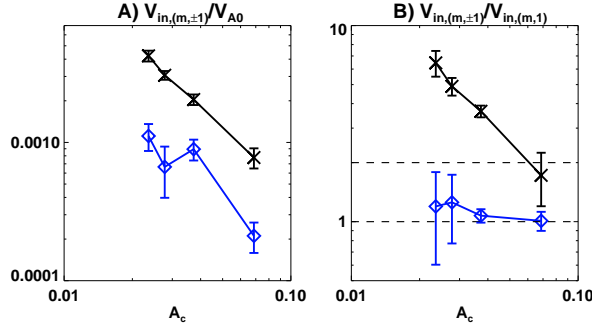


FIG. 9. Panel A): time-averaged inflow of diffusion regions on  $z = 0$  plane in double-layer simulations. Panel B): time-averaged inflow ratio of double-layer simulations to their correspondent single-layer simulations. Black lines with crosses are the measurements on the left of the diffusion region. Blue lines with diamonds are the measurements on the right of the diffusion region. Standard deviations are shown as error bars.

$(1, \pm 1)$  with  $A_c \sim 0.07$  is  $\sim 2$ . It means the inflow-outflow coupling is ineffective that the resultant inflow is roughly the superposition of the inflow into the present detecting diffusion region and the diverging outflow from the diffusion region on the other side of the current sheet. With a smaller distance between layers ( $m \geq 2$ ), an effective inflow-outflow coupling is built that the enhancement value exceeds 2 largely.

In comparison, it is shown in panel B) that the inflow in double-layer simulations from the right side is not effectively changed compared to single-layer simulations even when the inflow-outflow coupling is strong from the left side. Nonetheless, the entire diffusion region shows an increased potential in reconnection when the layers are closer to each other.

From our result in Sec.III A 1, we have found that the inflow-outflow coupling will trigger secondary tearing even if the original single tearing mode is stable to secondary tearing. In Fig.10, we compare the double-layer simulations  $(2, \pm 1)$ ,  $(4, \pm 1)$  and their correspondent single-layer simulations to see the local development of diffusion regions in the early stage. In the upper panels, it can be seen that the tearing mode  $(2, 1)$  is potentially vulnerable to the secondary tearing, while mode  $(4, 1)$  is secondary-tearing-stable. Both double-layer simulations  $(2, \pm 1)$  and  $(4, \pm 1)$  exhibit the character of secondary tearing that partition of current density peak can be seen from the lower panels.

The magnetic energy of energy modes calculated by Eq.(23) at a certain time for all double-layer simulations is plotted in Fig.11. The time slice for the double-layer simulation  $(1, \pm 1)$  is chosen when the overall magnetic energy dissipation rate reaches the first peak. The others are chosen when the final energy modes in the energy transfer reach their peaks. In the effective inflow-outflow coupling cases ( $m \geq 2$ ), a energy transfer path along the global guide field ( $k_z$ -direction, or along  $|n|$ ) can be seen. However, in the double-layer simulation  $(1, \pm 1)$ , the energy mainly goes along the 2D-like cascade path (yellow dashed line).

We explore the individual energy transfer paths for both double-layer simulations  $(2, \pm 1)$  and  $(4, \pm 1)$ . The energy

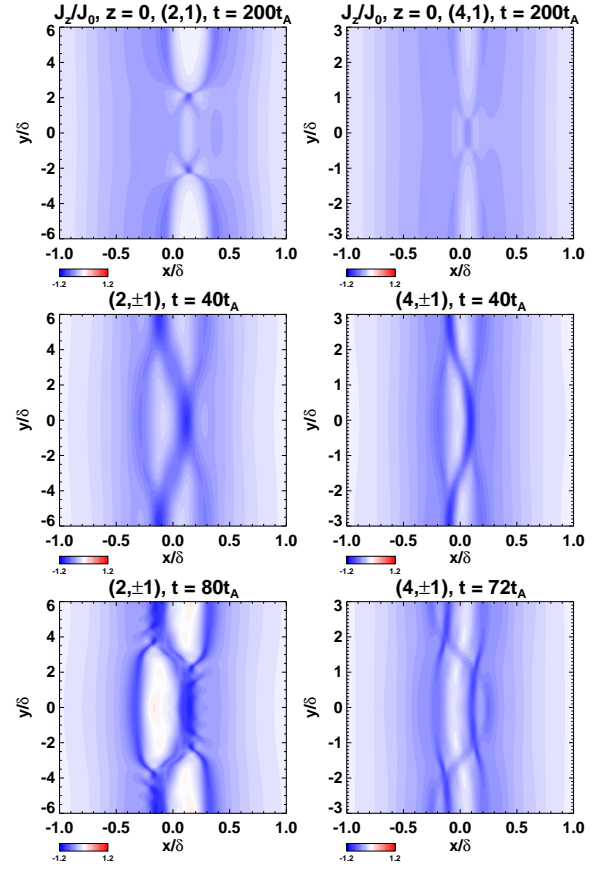


FIG. 10. Current density  $J_z$  contour plot for double-layer simulations  $(2, \pm 1)$ ,  $(4, \pm 1)$  and their correspondent single-layer simulations at different times on the anti-symmetric plane  $z = 0$ .

transfer rate of energy modes  $(2, 3)$  and  $(4, 3)$ , which are the first energy mode along  $|n|$  direction in the energy transfer, is plotted in Fig.12. The turquoise lines of  $(-2, 1) + (4, 2) \rightarrow (2, 3)$  in panel A and  $(-4, 1) + (8, 2) \rightarrow (4, 3)$  in panel B are similar paths to  $(-3, 1) + (6, 2) \rightarrow (3, 3)$  in Fig.7 panel C). All of them are dominant before the daughter modes are capable to grow themselves by extracting the energy from the background magnetic field.

Finally, we compare the overall magnetic energy dissipation rate calculated by Eq.(20) of all simulations (Fig.13). We measure at two different times. The first measurement is taken just before secondary tearing emerges. The second measurement is taken at the times the same as that in Fig.11.

In the understanding of the first measurement, we compare the overall magnetic energy dissipation rate of double-layer simulations over their correspondent single-layer simulations in panel A). Although the inflow-outflow coupling becomes more effective with decreasing  $A_c$ , the overall magnetic energy dissipation ratio exhibits a non-monotonic change with a peak around  $A_c \sim 0.035$ . Probably because the closest pair of the coupling has the shortest wavelength, they influence only a limited region near the central global sheet center. Therefore, the overall magnetic energy dissipation rate does not change

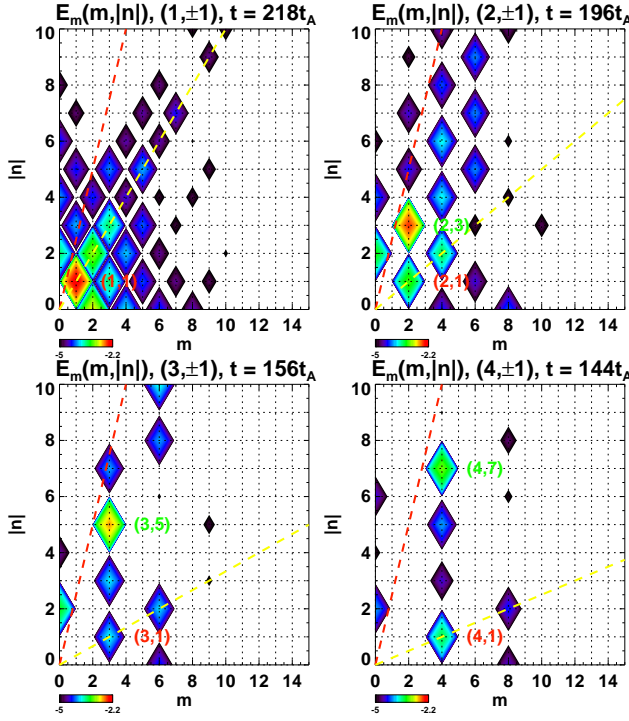


FIG. 11. Magnetic energy of energy modes calculated by Eq.(23) for all double-layer simulations. The original energy modes are labeled as red characters, while the green color represents the final energy mode in the energy transfer. The red dashed line is the asymptotic magnetic field orientation. The yellow dashed line is the 2D-like cascade path for initially perturbed modes. Colors are in the logarithmic scale.

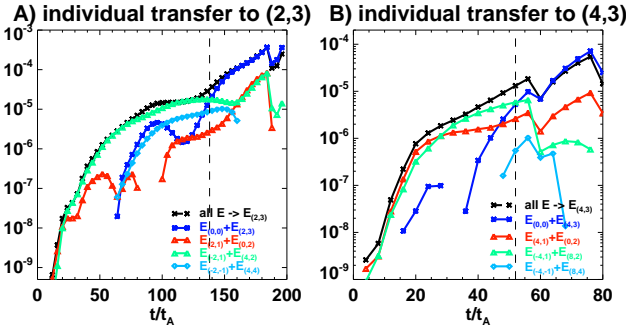


FIG. 12. Individual energy transfer rate of energy modes (2,3) and (4,3) in double-layer simulations (2,±1) and (4,±1), respectively. Black dashed lines at  $t = 138t_A$  in A) and  $t = 52t_A$  in B) are the starting time for the rapid growth of (2,3) and (4,3).

much compared to its single-layer counterpart. The absolute values of the overall magnetic energy dissipation rate of all double-layer simulations measured at two different times are shown in panel B). The double-layer simulation (1,±1) has the largest overall magnetic energy dissipation rate values than all other simulations, regardless of the time. Nonetheless, the overall magnetic energy dissipation rate in the second measurement shows that more effective inflow-outflow coupling

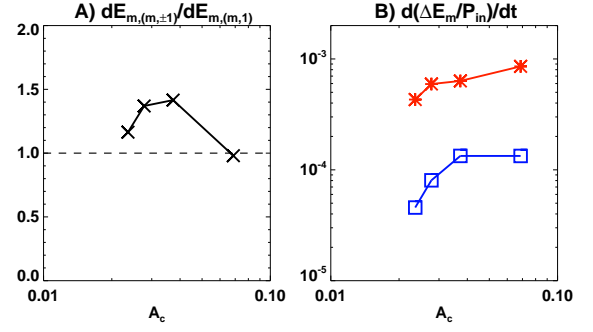


FIG. 13. Panel A): the overall magnetic energy dissipation rate ratio of double-layer simulations over their correspondent single-layer simulations just before secondary tearing emerges. The values are normalized by the initial overall magnetic energy dissipation rate ( $t \sim 0$ ). Panel B): the overall magnetic energy dissipation rate of double-layer simulations. The blue line with squares is the measurements just before secondary tearing emerges, the same as panel A). The red line with stars is the measurements selected at the same times as that in Fig.11.

will result in a higher enhancement of the overall magnetic energy dissipation rate compared to their first stage.

From our results above, we have found that the inflow-outflow coupling can be built when the relative distance between two reconnection layers is small. It can trigger secondary tearing, energy transfer to energy modes that grow outwardly and a faster overall magnetic energy dissipation rate compared to a single reconnection layer. The arguments are retested in the random-perturbation simulation group, which has a more general setup and different parameter ranges.

#### IV. SIMULATION RESULT II: RANDOM-PERTURBATION GROUP

The complicated structure in the random-perturbation group makes the quantitative analysis difficult, especially the local analysis as that in Sec.III A 1. Therefore, we only concentrate on the global character of this group.

We calculate the reconnection rate by measuring the reconnected flux growth rate, which follows the same method as that in Huang and Bhattacharjee<sup>3</sup>. The fastest reconnected flux growth rate before the boundaries start to interfere is shown in Fig.14. The reconnection rate in  $\alpha = 0.01$  is calculated at  $t = 1000t_A$ . In addition, we calculate the magnetic energy of energy modes. The simulations in which the energy transfer along the global guide field is found are labeled with circles. Otherwise, the simulations are labeled with crosses.

From our simulation result, the reconnection rate of the simulation subgroup with different diffusivity ( $\alpha = 0.1$ ) shows a weak dependence on the uniform diffusivity. The values are in the same order of magnitude as other spontaneous 3D reconnection studies with moderate global guide field strength<sup>4,5</sup>. All simulations in this subgroup exhibit an energy transfer along the global guide field. A qualitative examination shows that they basically follow the same sce-

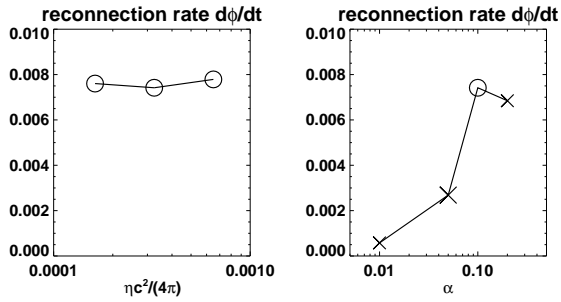


FIG. 14. Reconnection rate calculated by the fastest reconnected flux growth rate for each subgroup.

nario as what we have found in the eigenmode-perturbation group. However, unlike that in the eigenmode-perturbation group, multiple reconnection layers (more than 2) emerge in the initial state due to the implementation of a random velocity field. The distance between layers on the same side of the central global current sheet is closer than the distance between layers from either side of the sheet. Therefore, the layers interact with each other on either side of the central global current sheet first. When they grow thick enough, they interact across the sheet center and achieve fast global reconnection.

In comparison, the reconnection rate shows a non-monotonical dependence on the uniform global guide field. It seems that there is a preferred window selected by the global guide field for fast energy dissipation in our system. When the guide field is small that  $\alpha < 0.1$ , the global reconnection rate reduces with the global guide field strength.

In the case with  $\alpha = 0.01$ , reconnection happens only near the central global current sheet center before  $t = 1000t_A$ . Energy modes  $(1,1)$ ,  $(1,-1)$  and  $(1,0)$  are dominant before  $t \sim 500t_A$ . Due to the resonance condition of the closed box, 3D energy modes  $(1,1)$  and  $(1,-1)$  are growing close to the central global current sheet center. No energy transfer along the global guide field is found. Thus no new reconnection layer grow further away from the center. As we have shown in Sec.III B, the global reconnection rate is low if the reconnection layers are confined near the sheet center. On the other hand, from  $t \sim 500t_A$  until the end of the simulation ( $t = 1000t_A$ ), the dominant energy modes are 3D energy modes with  $m = 0$ . These modes do not participate in the reconnection thus the global reconnection decreases from  $t \sim 600t_A$ . The reconnection rate increases again from  $t \sim 900t_A$  due to the growth of 2D energy mode  $(1,0)$ . There remains a possibility that the reconnection can accelerate further after  $1000t_A$ . Since the growth rate of energy mode  $(1,0)$  is  $1/4$  of that in the random perturbation simulation with  $\alpha = 0.1$  in the similar stage, we believe that the reconnection rate enhancement might not be considerable.

In the simulations  $\alpha = 0.05$  and  $\alpha = 0.2$ , the distance between initially emerged reconnection layers is larger than the distance between reconnection layers in  $\alpha = 0.1$  case. It is possible that the diffusion regions on the layers in  $\alpha = 0.05$  and  $\alpha = 0.2$  hardly couple so no energy transfer along the global guide field is achieved. Therefore, the global recon-

nection is expected to be slow following our scenario.

However,  $\alpha = 0.2$  case reaches a global reconnection rate that is similar to  $\alpha = 0.1$  cases. This is probably related to the closed boundary condition. In our closed system, the global magnetic field structure ends with the structure that corresponds to the energy modes with the longest wavelengths that can be reached in the system, namely 2D energy mode  $(1,0)$ , 3D energy modes  $(1,1)$  and  $(1,-1)$ . By Eq.(18), the  $x$ -positions of energy modes  $(1,1)$  and  $(1,-1)$  in  $\alpha = 0.2$  case are the largest among all simulation cases. Since the energy modes  $(1,1)$  and  $(1,-1)$  are close to the asymptotic magnetic field, they can efficiently convert the magnetic energy.

## V. DISCUSSION

One global picture of the spontaneous 3D reconnection was given in Beresnyak<sup>5</sup>. This work proposed that turbulence gradually builds and expands the whole current sheet, finally produces global 2D-like bi-directional inflows and outflows. In our study, we showed how new energy modes, which grow new reconnection layers, are produced outwardly. This process explains the global current sheet expansion stage. Meanwhile, the nonlinear coupling of the pre-existing modes creates new modes and builds the turbulent state, as more and more energy modes are activated seen from 2D energy spectrum in Sec.III A 2. In the turbulence reconnection picture<sup>9</sup>, the field lines are thought to wander around inside the whole current sheet and gradually release the energy by continuous reconnection at different positions. We describe this wandering motion as the inflow-outflow coupling of diffusion regions on adjacent reconnection layers. The physics of the inflow-outflow coupling was examined locally in detail. In this sense, we have given a clear physical picture of the turbulence reconnection process, from the viewpoint of the diffusion region development and the interaction between reconnection layers.

All our present simulation results are based on the simulation in a closed box. It is often the case that the system is open on both ends or at least one. When the system is open, the reconnected structures can be removed from the current sheet by the global outflow. From our result in a closed box, the growth of new energy modes away from the current sheet center is important in enhancing the global reconnection efficiency. It requires  $\sim 100t_A$  to grow a new energy mode by observing Fig.6 in our present simulation setup. If we assume the 2D outflow is in the magnitude of  $v_{A0}$ , then the global current sheet must be longer than  $100\delta$  to ensure that the new energy modes can be generated with the present structure. Whether our scenario can be retrieved in an open system needs to be examined in a simulation box with open boundaries.

From the simulation result of the global guide field subgroup, it is found that the coexistence of multiple reconnection layers in a closed box does not always lead to a fast global reconnection. This is due to the large distance between initially emerged reconnection layers, as some tearing modes are suppressed by the closed boundary condition. When the simulation box becomes open, the tearing modes are free to grow. If the distance between the layers on which tearing modes

grow is small enough to build the inflow-outflow coupling, the global current sheet might follow our scenario to reach a fast overall reconnection. However, if the distance between layers is in the same magnitude as the thickness of the diffusion layer of a tearing mode, this bunch of reconnection layers possibly behaves like a thick layer. How the reconnection develops in such a case needs further investigation.

Previous simulation results suggest that the physics in the reconnecting global current sheet changes with the applied global guide field strength<sup>2,4</sup>. We believe that our scenario is applicable directly to describe the 3D reconnection in a global current sheet with a moderate global guide field ( $\alpha > 0$ ). Meanwhile, since only one reconnection layer at the global current sheet center is allowed to grow when  $\alpha \sim 0$ , the depletion of reconnection layers on which 3D energy modes grow implies a slower reconnection by our analysis. Therefore, we are capable to give a consistent theory to explain the reconnection rate difference in current sheets with different global guide field strengths. On the other hand, how the turbulence accelerates the 3D reconnection in a global current sheet with  $\alpha = 0$  is still not fully understood. It was thought that Kelvin–Helmholtz-like 3D instability which breaks the Sweet-Parker<sup>31,32</sup> type diffusion region into filaments is important in enhancing the global reconnection rate<sup>2</sup>. Quantitative analysis is needed to have a concrete conclusion.

The diffusivities applied in our simulation are much higher than the astronomical value. From our present diffusivity subgroup result, a fast reconnection is expected if the diffusivity is even lower. However, the developing time to reach a fast reconnection might be diffusivity-dependent. Assume that the inflow-outflow coupling between diffusion regions is a universal phenomenon. The tearing mode needs time to grow into an amplitude large enough to start the inflow-outflow coupling effectively across the global current sheet. The linear growth rate of the tearing mode is reversely scaled to the diffusivity<sup>33,34</sup>. Then it is highly possible that it takes a long time for a system to develop the inflow-outflow coupling when the diffusivity is small. Once it is built, the inflow-outflow coupling changes the spontaneous reconnection into the driven regime locally<sup>35</sup>. Theoretically, the local reconnection is less dependent on the diffusivity in the driven reconnection but rather relies on the inflow electric field ( $E_{\text{in}} \sim v_{\text{in}} B_{\text{in}}/c$ )<sup>36,37</sup>. Thus it is possible that the global reconnection becomes less dependent on the diffusivity due to the local driven reconnection that spreads all over the global current sheet. Whether this holds true in a slowly diffusing magnetic field is unclear and requires studies set with much lower diffusivity.

## VI. CONCLUSION

In our present study, we found a growth of new energy modes near the global current sheet boundaries in spontaneous 3D reconnection. The emergence of the new modes comes from the interaction of reconnection layers closer to the global current sheet center. The global fast magnetic energy dissipation is achieved when reconnection layers expand across the

current sheet, while individual diffusion regions on different reconnection layers build an inflow-outflow coupling that supports a fast local reconnection. As a whole, we present a detailed explanation of the development of diffusion regions in a current sheet when the turbulence is building. We also show how important 3D energy modes contribute to the overall energy dissipation.

Although our simulations are executed in a closed box, there remains a possibility that similar processes could be achieved in an open system. Further examination with a larger box or with open boundaries should be done to confirm our picture. On the other hand, our present diffusivity is still far higher than the astronomical value. Lundquist number larger than  $10^7$  is required to observe a sufficient energy spectrum. Huge simulation on the topic of reconnection is always required to explain the enormous energy release in the astronomical phenomenon.

## ACKNOWLEDGMENTS

Numerical computations were [in part] carried out on Cray XC30 at Center for Computational Astrophysics, National Astronomical Observatory of Japan. Numerical computations were [in part] carried out on Cray XC50 at Center for Computational Astrophysics, National Astronomical Observatory of Japan. Takaaki Yokoyama is supported by JSPS KAKENHI Grant: JP15H03640.

- <sup>1</sup>G. Kowal, A. Lazarian, E. T. Vishniac, and K. Otmianowska-Mazur, “Numerical Tests of Fast Reconnection in Weakly Stochastic Magnetic Fields,” *The Astrophysical Journal* **700**, 63–85 (2009), arXiv:0903.2052 [astro-ph.GA].
- <sup>2</sup>J. S. Oishi, M.-M. Mac Low, D. C. Collins, and M. Tamura, “Self-generated Turbulence in Magnetic Reconnection,” *The Astrophysical Journal Letters* **806**, L12 (2015), arXiv:1505.04653 [astro-ph.SR].
- <sup>3</sup>Y.-M. Huang and A. Bhattacharjee, “Turbulent Magnetohydrodynamic Reconnection Mediated by the Plasmoid Instability,” *The Astrophysical Journal* **818**, 20 (2016), arXiv:1512.01520 [physics.plasm-ph].
- <sup>4</sup>G. Kowal, D. A. Falceta-Gonçalves, A. Lazarian, and E. T. Vishniac, “Statistics of Reconnection-driven Turbulence,” *The Astrophysical Journal* **838**, 91 (2017), arXiv:1611.03914.
- <sup>5</sup>A. Beresnyak, “Three-dimensional Spontaneous Magnetic Reconnection,” *The Astrophysical Journal* **834**, 47 (2017), arXiv:1301.7424 [astro-ph.SR].
- <sup>6</sup>T. K. M. Nakamura, R. Nakamura, Y. Narita, W. Baumjohann, and W. Daughton, “Multi-scale structures of turbulent magnetic reconnection,” *Physics of Plasmas* **23**, 052116 (2016).
- <sup>7</sup>N. F. Loureiro and S. Boldyrev, “Collisionless reconnection in magnetohydrodynamic and kinetic turbulence,” *The Astrophysical Journal* **850**, 182 (2017).
- <sup>8</sup>W. H. Matthaeus and S. L. Lamkin, “Rapid magnetic reconnection caused by finite amplitude fluctuations,” *Physics of Fluids* **28**, 303–307 (1985).
- <sup>9</sup>A. Lazarian and E. T. Vishniac, “Reconnection in a Weakly Stochastic Field,” *The Astrophysical Journal* **517**, 700–718 (1999), astro-ph/9811037.
- <sup>10</sup>P. Goldreich and S. Sridhar, “Toward a theory of interstellar turbulence. 2: Strong Alfvénic turbulence,” *The Astrophysical Journal* **438**, 763–775 (1995).
- <sup>11</sup>S. Boldyrev and N. F. Loureiro, “Magnetohydrodynamic Turbulence Mediated by Reconnection,” *The Astrophysical Journal* **844**, 125 (2017), arXiv:1706.07139 [physics.plasm-ph].
- <sup>12</sup>A. Mallet, A. A. Schekochihin, and B. D. G. Chandran, “Disruption of sheet-like structures in Alfvénic turbulence by magnetic reconnection,”

- Monthly Notices of the Royal Astronomical Society **468**, 4862–4871 (2017), arXiv:1612.07604 [astro-ph.SR].
- <sup>13</sup>A. A. Galeev and L. M. Zelenyi, “Model of magnetic-field reconnection in a plane layer of collisionless plasma,” *ZhETF Pisma Redaktsiiu* **25**, 407–411 (1977).
- <sup>14</sup>M. Onofri, L. Primavera, F. Malara, and P. Veltri, “Three-dimensional simulations of magnetic reconnection in slab geometry,” *Physics of Plasmas* **11**, 4837–4846 (2004).
- <sup>15</sup>S. Landi, P. Londrillo, M. Velli, and L. Bettarini, “Three-dimensional simulations of compressible tearing instability,” *Physics of Plasmas* **15**, 012302 (2008).
- <sup>16</sup>S. Wang, T. Yokoyama, and H. Isobe, “Three-dimensional MHD Magnetic Reconnection Simulations with a Finite Guide Field: Proposal of the Shock-evoking Positive-feedback Model,” *The Astrophysical Journal* **811**, 31 (2015), arXiv:1508.03140 [astro-ph.SR].
- <sup>17</sup>K. Shibata and S. Tanuma, “Plasmoid-induced-reconnection and fractal reconnection,” *Earth, Planets, and Space* **53**, 473–482 (2001), astro-ph/0101008.
- <sup>18</sup>N. F. Loureiro, S. C. Cowley, W. D. Dorland, M. G. Haines, and A. A. Schekochihin, “X-Point Collapse and Saturation in the Nonlinear Tearing Mode Reconnection,” *Physical Review Letters* **95**, 235003 (2005), physics/0507206.
- <sup>19</sup>Y.-M. Huang and A. Bhattacharjee, “Scaling laws of resistive magnetohydrodynamic reconnection in the high-Lundquist-number, plasmoid-unstable regime,” *Physics of Plasmas* **17**, 062104–062104 (2010), arXiv:1003.5951 [physics.plasm-ph].
- <sup>20</sup>D. Grasso, D. Borgogno, and F. Pegoraro, “Secondary instabilities in two- and three-dimensional magnetic reconnection in fusion relevant plasmas,” *Physics of Plasmas* **14**, 055703 (2007).
- <sup>21</sup>T. Kudoh, K. Shibata, and R. Matsumoto, “2. 5D Nonsteady MHD Simulations of Magnetically Driven Jets from Accretion Disks by Using the CIP-MOCCT Method<sup>CD</sup>,” in *Numerical Astrophysics*, Astrophysics and Space Science Library, Vol. 240, edited by S. M. Miyama, K. Tomisaka, and T. Hanawa (1999) p. 203.
- <sup>22</sup>A. Lapidus, “A Detached Shock Calculation by Second-Order Finite Differences,” *Journal of Computational Physics* **2**, 154–177 (1967).
- <sup>23</sup>B. D. Jemella, M. A. Shay, J. F. Drake, and B. N. Rogers, “Impact of Frustrated Singularities on Magnetic Island Evolution,” *Physical Review Letters* **91**, 125002 (2003).
- <sup>24</sup>A. Bhattacharjee, Y.-M. Huang, H. Yang, and B. Rogers, “Fast reconnection in high-Lundquist-number plasmas due to the plasmoid instability,” *Physics of Plasmas* **16**, 112102 (2009), arXiv:0906.5599 [physics.plasm-ph].
- <sup>25</sup>N. F. Loureiro, R. Samtaney, A. A. Schekochihin, and D. A. Uzdensky, “Magnetic reconnection and stochastic plasmoid chains in high-Lundquist-number plasmas,” *Physics of Plasmas* **19**, 042303–042303 (2012), arXiv:1108.4040 [astro-ph.SR].
- <sup>26</sup>T. Shibayama, K. Kusano, T. Miyoshi, T. Nakabou, and G. Vekstein, “Fast magnetic reconnection supported by sporadic small-scale Petschek-type shocks,” *Physics of Plasmas* **22**, 100706 (2015).
- <sup>27</sup>K. Kusano and T. Sato, “Non-linear coupling effects on the relaxation process in the reversed field pinch,” *Nuclear Fusion* **27**, 821 (1987).
- <sup>28</sup>R. B. Dahlburg, S. K. Antiochos, and T. A. Zang, “Secondary instability in three-dimensional magnetic reconnection,” *Physics of Fluids B* **4**, 3902–3914 (1992).
- <sup>29</sup>S. A. Orszag and A. T. Patera, “Secondary instability of wall-bounded shear flows,” *Journal of Fluid Mechanics* **128**, 347–385 (1983).
- <sup>30</sup>R. S. Steinolfson, “Energetics and the resistive tearing mode - Effects of Joule heating and radiation,” *Physics of Fluids* **26**, 2590–2602 (1983).
- <sup>31</sup>P. A. Sweet, “The Neutral Point Theory of Solar Flares,” in *Electromagnetic Phenomena in Cosmical Physics*, IAU Symposium, Vol. 6, edited by B. Lehnert (1958) p. 123.
- <sup>32</sup>E. N. Parker, “Sweet’s Mechanism for Merging Magnetic Fields in Conducting Fluids,” *Journal of Geophysical Research* **62**, 509–520 (1957).
- <sup>33</sup>H. P. Furth, J. Killeen, and M. N. Rosenbluth, “Finite-Resistivity Instabilities of a Sheet Pinch,” *Physics of Fluids* **6**, 459–484 (1963).
- <sup>34</sup>B. Coppi, R. Galvao, R. Pellat, M. Rosenbluth, and P. Rutherford, “Resistive internal kink modes,” *Fizika Plazmy* **2**, 961–966 (1976).
- <sup>35</sup>P. L. Pritchett, Y. C. Lee, and J. F. Drake, “Linear analysis of the double-tearing mode,” *Physics of Fluids* **23**, 1368–1374 (1980).
- <sup>36</sup>T. Sato and T. Hayashi, “Externally driven magnetic reconnection and a powerful magnetic energy converter,” *Physics of Fluids* **22**, 1189–1202 (1979).
- <sup>37</sup>H. Kitabata, T. Hayashi, T. Sato, and Complexity Group, “Impulsive Nature in Magnetohydrodynamic Driven Reconnection,” *Journal of the Physical Society of Japan* **65**, 3208 (1996).